Helmholtz-Zentrum Dresden-Rossendorf (HZDR)

Edge and Point-Defect Induced Electronic and Magnetic Properties in Monolayer PtSe$_2$

Li, J.; Joseph, T.; Ghorbani Asl, M.; Kolekar, S.; Krasheninnikov, A.; Batzill, M.;

Edge and Point-Defect Induced Electronic and Magnetic Properties in Monolayer PtSe$_2$

Jingfeng Li,[1,] Thomas Joseph,[2] Mahdi Ghorbani-Asl,[2] Sadhu Kolekar,[1] Arkady V. Krasheninnikov,[2,3]

Matthias Batzill[1,*]

[1] Department of Physics, University of South Florida, Tampa, FL 33620, USA
[2] Helmholtz-Zentrum Dresden-Rossendorf, Institute of Ion Beam Physics and Materials Research, 01328 Dresden, Germany
[3] Department of Applied Physics, Aalto University, P.O. Box 11100, 00076 Aalto, Finland

[*] Corresponding author: Matthias Batzill; e-mail: mbatzill@usf.edu

TOC text:

Compared to multilayers, monolayer PtSe$_2$ exhibits a unique gap opening which enables the detailed characterization of defect induced electronic states. Pt-vacancies whose spin polarized nature has been linked to magnetic ordering are shown to be rare in the material. Instead, a metallization of zigzag edges is discovered with spin polarized edge states that may enable magnetic modifications of PtSe$_2$ nanomaterials.

TOC-graphics:
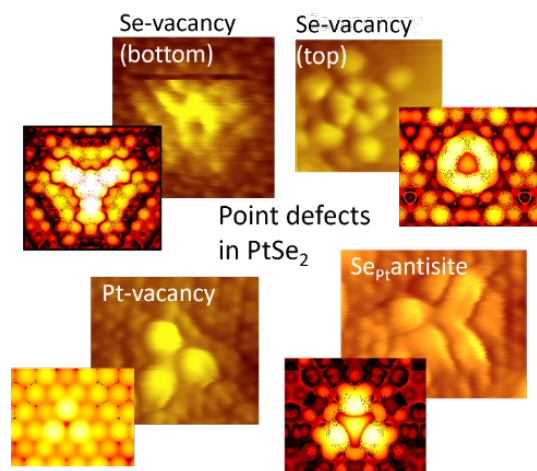
Abstract:

Edges and point defects in layered dichalcogenides are important for tuning their electronic and magnetic properties. By combining scanning tunneling microscopy (STM) with density functional theory (DFT), the electronic structure of edges and point defects in 2D-PtSe$_2$ are investigated where the 1.8 eV-band gap of monolayer PtSe$_2$ facilitates the detailed characterization of defect-induced gap states by STM. The stoichiometric zigzag edge terminations are found to be energetically favored. STM and DFT shows that these edges exhibit metallic one-dimensional states with spin polarized bands. Various native point defects in PtSe$_2$ are also characterized by STM. A comparison of the experiment with simulated images enables identification of Se-vacancies, Pt-vacancies, and Se-antisites as the dominant defects in PtSe$_2$. In contrast to Se- or Pt- vacancies, the Se-antisites are almost devoid of gap states. Pt-vacancies exhibit defect induced states that are spin polarized, emphasizing their importance for inducing magnetism in PtSe$_2$. The atomic-scale insights into defect-induced electronic states in monolayer PtSe$_2$ provide the fundamental underpinning for defect engineering of PtSe$_2$-monolayers and the newly identified spin-polarized edge states offer prospects for engineering magnetic properties in PtSe$_2$ nanoribbons.

1. Introduction

Layered Pt dichalcogenides have attracted interest for a variety of potential applications in electrocatalysis or as electronic materials.[1,2,3,4,5,6,7,8,9,10,11] Moreover, defect-induced magnetism was recently found in $PtSe_2$ that persists to the monolayer regime.[12,13] Point defects and other lattice imperfections including edges are important not only for adding magnetism to $PtSe_2$, but also for controlling its chemical functionalities[14,15] that are known to be important in other layered transition metal dichalcogenides (TMDs).[16] Metallic edges are documented for semiconducting group VIB-dichalcogenides in the H-phase, most prominently for MoS_2.[17,18,19] It has been shown that these edges are important for electrochemical functionalities in these materials. In the 1T' family of TMDs, the topologically protected edge states in monolayer 1T'-WSe_2 and WTe_2 give rise to quantum spin Hall state[20,21] which makes these edge states a potential candidate for topological field effect transistors.[22] While these edge states are well-characterized in group VIB TMDs, the structure and electronic properties of the electronically very different noble metal dichalcogenides have not yet been studied. However, as we show here, the edge properties of these materials provide another exciting system for one dimensional edge states, which are distinct from other TMDs due to their spin-polarized nature.

Layered TMDs have been demonstrated to exhibit changes in their electronic properties if reduced to a single layer.[23,24,25,26,27,28,29,30,31,32,33,34] In Pt-dichalcogenides these modifications are very pronounced, while bulk and few layer materials are known to be metallic, single molecular layers of $PtSe_2$ or $PtTe_2$ become semiconductors with a band gap well above one eV, in the case of $PtSe_2$.[35,36,37,38,39,40] This extraordinary opening of a considerable band gap for the monolayer will also affect the electronic structure of the defective material. While in multilayer samples defect states may hybridize with the electronic states of the pristine material, in monolayers these defect states normally lie within the band gap. Importantly, the presence of the band gap in the pristine monolayers enables the characterization of defect-induced states by scanning tunneling spectroscopy. Thus, the synthesis of monolayer samples is critical for the characterization of defect induced electronic states and to advance our understanding of defect-controlled properties in $PtSe_2$. Both native point defects, as well as lattice discontinuities at edges, can induce band gap states. Edges of 2D crystals have broken covalent bonds and may be considered to be 1D-equivalent to the surfaces of 3D crystals. Similar to 3D crystals, broken covalent bonds at the edges of 2D crystals may lead to new electronic states.[41]

In this work, we characterize the structure, composition, and electronic properties of monolayer $PtSe_2$ with edges as well as point defects. To achieve this, we prepare monolayer samples by molecular beam

epitaxy and use scanning tunneling microscopy (STM) and spectroscopy (STS) to study the properties of atomic-scale defects. By matching experimental measurements with the results of density functional theory (DFT) calculations, we infer detailed structural and compositional information of the defects present in $PtSe_2$, which govern the properties of defective $PtSe_2$ systems. These studies provide the foundation for controlled defect engineering of $PtSe_2$ and most importantly the newly discovered spin-polarized edge states in $PtSe_2$ provide prospects for new one-dimensional magnetic devices.

2. Results and discussion

DFT simulations[37] have predicted strong dependence of the band gap for $PtSe_2$ on the number of layers in the sample, and we indeed found the layer dependence of the band gap of these Pt-dichalcogenides as obtained by STS.[35] These measurements demonstrated that monolayer $PtSe_2$ has a band gap of 1.8 eV. As discussed in ref [35], depending on the exchange and correlation (XC) functional used in the DFT calculations and the flavor of the post-DFT GW approaches, the calculations may over- or under-estimate the band gap. Here we use DFT with the PBE XC functional,[42] which yields the band gap of monolayer $PtSe_2$ to be 1.2 eV, which is significantly smaller than the experimental gap. Also, the Fermi-level position may be different in the calculations from the experiments. In the experiments, we observe an n-type doped sample with the Fermi-level around 0.6 eV below the conduction band minimum. This doping of the pristine monolayer is likely associated with the $PtSe_2$/HOPG interface.[35] The DFT calculations are done on free-standing $PtSe_2$, and for defective $PtSe_2$ system the Fermi-level lies at the highest occupied defect state. Differences in the calculated and experimentally determined band gaps and Fermi-level positions need to be considered when comparing the theoretical results with the experiments. In the following, we first investigate lattice discontinuities at step edges of monolayer-thick $PtSe_2$ islands. After that we turn to point defects in the monolayers.

2.1 Edge properties

Figure 1 (a) shows a large-scale STM image of the MBE grown $PtSe_2$ islands. Most of the islands are monolayers, but some bilayer regions are also present. The inset shows an atom-resolved image along a step edge of a monolayer terrace with the line profile along the indicated direction shown in Figure 1(b). Most of the edges of the $PtSe_2$ islands are oriented by multiples of 60˚ relative to each other, suggesting a preference for a single edge orientation, because of the 120˚ rotational symmetry of the 1T crystal structure. Figure 1(c) shows the schematic edge terminations for both armchair- or zigzag- edges. Cutting the crystal structure along the armchair direction only allows for one possible termination without edge

4

reconstruction, which results in a stoichiometric edge, *i.e.*, a PtSe$_2$ composition. In contrast, the zigzag direction can be cut along three different lines resulting in edges with varying compositions as illustrated in Figure 1(b). The edge labeled 50% Se has the stoichiometric termination, while the edge labeled 0% Se is Pt-rich, and the edge labeled 100% Se is Se-rich. To determine the energetic preference for different edge orientations and terminations, we calculated the formation energies of the edges as functions of Se-chemical potential, shown in Figure 2. For the stoichiometric edges the formation energy for zigzag edges is lower than that for armchair edges. Also, a Wulff construction (shown in the inset of Figure 2) of the 2D equilibrium island shape, using the calculated formation energies for the stoichiometric edge terminations, indicate that an equilibrium island would be entirely made up of zigzag edges with the energy for the armchair edge just outside of the equilibrium shape. The formation energy of the armchair edge is by a coincidence just a factor of ~1/cos 30° larger than that of the zigzag edge, which is the border-line condition in order to be part of the equilibrium island shape. The preference for a single edge orientation is also consistent with the STM images.
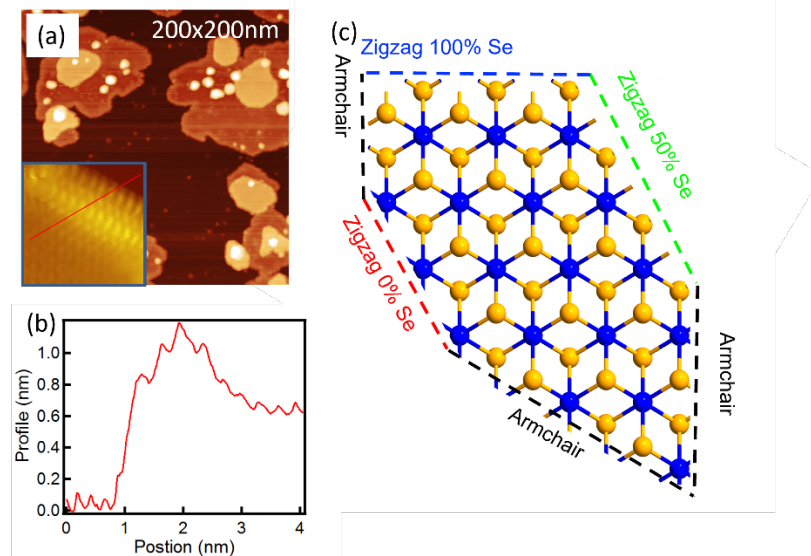

Figure 1: STM images and a schematic illustration of edges of PtSe$_2$ nanoislands grown by MBE on a HOPG substrate. Large scale STM image in (a) shows the PtSe$_2$ island morphology with the edges exhibiting a bright contrast. The inset shows a high resolution STM image of an edge with the line profile along the indicated direction displayed in (b). The schematic of possible edge terminations is shown in (c). Truncated crystals along the armchair direction only have one possible composition, while the zigzag edge can be truncated with three different possible compositions as indicated in panel (c).

For zigzag edges, different edge terminations are possible. Naturally, the non-stoichiometric edge terminations are dependent on Se chemical potential, as shown in Figure 2. The Se-deficient edge is always much higher in energy and thus unlikely to form. The Se-rich edge termination on the other hand, becomes lower in energy for very high values of Se chemical potential. The latter, however, is hardly possible under UHV growth conditions. Therefore, the most likely edge termination is the zigzag stoichiometric edge (50% Se).
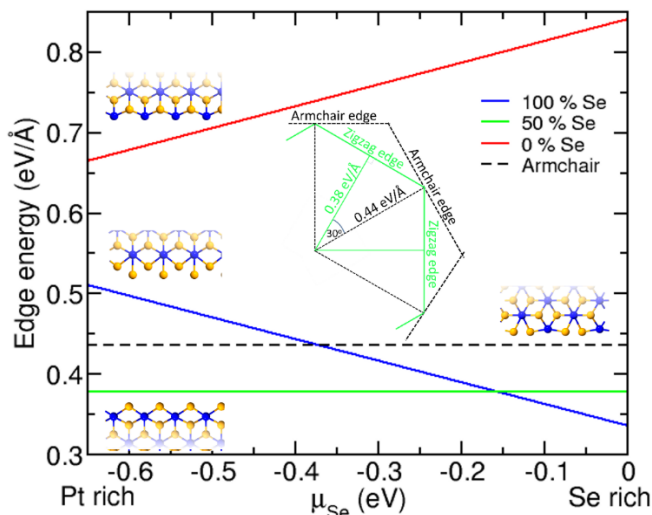

Figure 2: Calculated edge energies as functions of selenium chemical potential. The energy of a stoichiometric armchair edge is indicated by the black, dashed line. The three different edge stoichiometries for the zigzag edge are shown as solid lines, with the same colors as in Figure 1 (c). The inset presents a Wulff-construction of the equilibrium crystal shape, obtained by using the calculated edge energies for the stoichiometric zigzag and armchair edges.

To verify the edge termination, atomically resolved STM images are compared to the simulated STM images of different zigzag edge terminations. First, we point out that atomic resolution images indeed show that edges are zigzag oriented. The atomically resolved experimental images of the edge indicate that the brightest contrast is found away from the edge in the third Se-row, as shown from the line profile in Figure 1 (b) and displayed in Figure 3 as the red dashed lines. The experimental image and line profile are compared to simulated STM images for different edge terminations. In addition to the edge composition, two other configurations are possible for each composition with the terminating Se either in the top or bottom layer. For different compositions, the simulated STM images for the two configurations are shown in Figure 3, and the resulting line profiles are displayed together with the experimentally obtained profile. From the comparison, we can clearly exclude the presence of Pt-

terminated step edges (0% Se). The best agreement between the experiment and simulation is obtained for the stoichiometric edge (50% Se) and the terminating Se-atom in the bottom layer, *i.e.*, Se atoms pointing towards the substrate. Just from the comparison of the line profiles, it is not possible to entirely exclude the Se-rich termination with terminating Se atoms in the top layer. However, it is unlikely to have the Se-rich conditions in vacuum to make this configuration favorable. Thus, from a combination of *ab-initio* thermodynamics arguments and a comparison of the experimental STM contrast with the simulated STM images we conclude that the observed edges are stoichiometric with the terminating Se-atoms located at the interfaces with the graphite substrate.
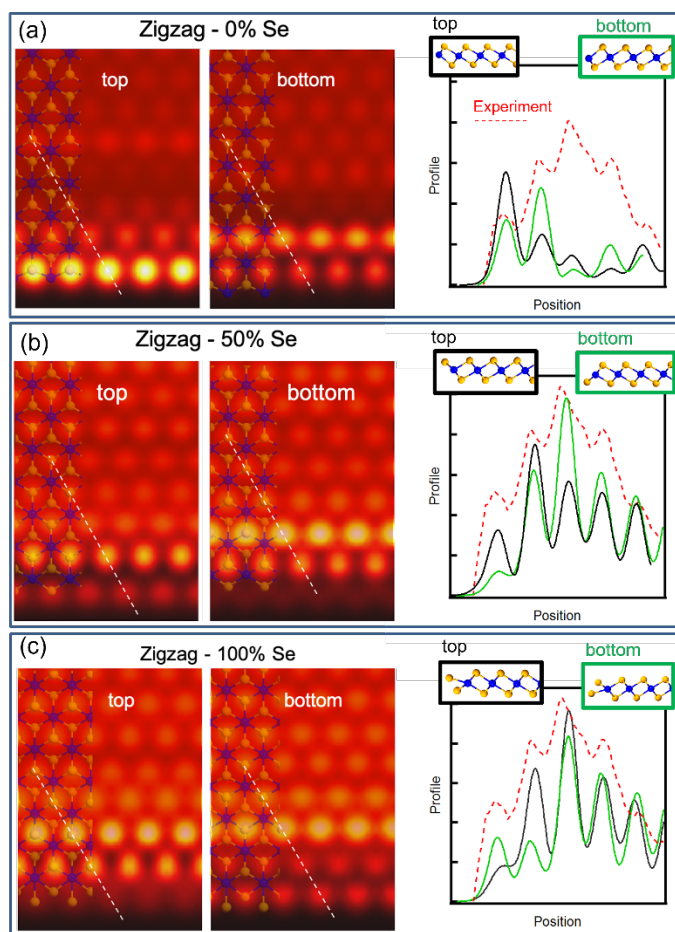

Figure 3: Simulated STM contrast for different zigzag edge configurations for (a) Pt-terminated edges, (b) stoichiometric edges, and (c) Se-rich edges. Two configurations are calculated for all three edge terminations with the terminating Se-atoms either in the top or bottom layer. The simulated line profiles along the direction indicated by the lines in the simulated images are compared to the experimental line profile (red dashed line) on the right side of the figure.

The brighter contrast of the edge may imply higher density of electronic states, in particular band gap states that enhance the tunneling probability at step edges. To quantify this, we used STS to probe the density of states in the vicinity of the step edges. Figure 4 shows the spectra as a function of distance from the step edge. Directly at the step edge, the band gap is completely closed indicating that the edge is metallic. Away from the step edge a band gap is present, with the value approaching that for the pristine terraces (~ 1.8 eV) around 2 nm away from the edge. The variation of the conduction band minimum (CBM) and valence band maximum (VBM) as a function of distance away from the edge is plotted in Figure 4(c). Away from the step edge, the $PtSe_2$ monolayer is slightly n-type doped (the Fermi level is closer to the CBM) in agreement with our previous reports for the $PtSe_2$/HOPG interface.[35] Metallic band gap states at the edge suggest that the Fermi-level is pinned close to the charge neutrality level of these edge states, similar to the Fermi-level pinning at the surface states of 3D semiconductor surfaces. The closing of the band gap at the edge agrees with the results of the DFT calculations shown in Figure 4 (d,e), which indicate that new bands in the gap are formed. The electronic structure calculations show that both edges create the same states in the form of two pairs of nearly degenerate bands which are well separated from the bulk states as shown in Figure S1. Moreover, according to the spin-polarized calculations, the VBM and CBM nearly touch each other in only one point in one of the spin channels (the band gap is about 0.1 eV), while there is a considerably larger gap in the other channel, so that the system can be referred to as a spin gapless semiconductor. This also suggests that a net magnetic moment may be obtained at these edges if the Fermi-level is shifted by *p*-type doping. In the calculations, a high density of states is observed at or just below the Fermi level, in agreement with the experimental dI/dV spectra (red arrow). Another peak in the density of the occupied states indicated by the green arrow is also identified in both the calculated DOS and the experimental data. These two states are separated~ 0.2-0.3 eV. Two-unit cells away from the edge, a band gap is clearly seen in the theoretical local density of states with band gap states indicated by the light and dark blue arrows in Figure 4d. These gap states may be correlated to the measured states in STS. At 4-unit cells from the edge the calculations indicate a band gap which is very close to the value of that of a pristine $PtSe_2$ monolayer. The fact that in the experiments the full opening of the gap is observed further away from the edge is possibly attributed to electron screening effects by the edge states that cause a closing of the gap in the edge vicinity. Similar gap closings have also been observed in the vicinity of the metallic grain boundaries in other 2D semiconductors[43,44] and in group VIB TMDs as already discussed above.

While all the studies are performed under ultraclean UHV conditions to ensure the integrity of the samples, it is interesting to point out the air-stability of the samples and edges as it does affect applications

and potential future investigations of edge properties. In our studies we exposed samples to air and kept them under ambient conditions for one hour and reintroduced the sample into UHV for STM characterization. Only a mild vacuum annealing to 200 ˚C is needed to remove adsorbates and re-establish clean imaging conditions. The edge properties before and after air exposure are indistinguishable, indicating the air stability not just of the basal plane but also of the edges. This suggests that this material is suitable for further non-vacuum studies of their edge states.
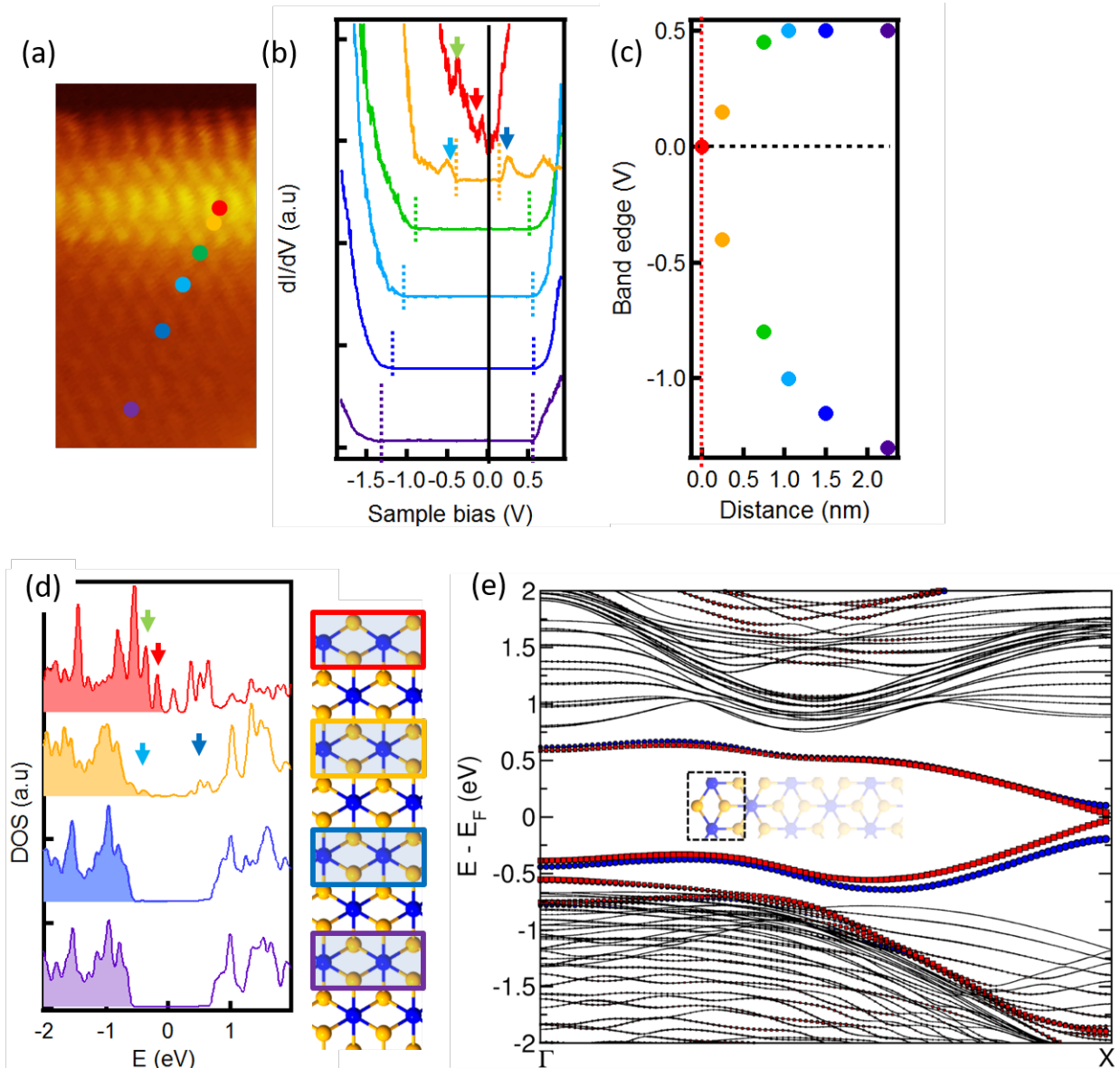

Figure 4: Electronic structure of zigzag step edge. Points at which STS measurements were taken are indicated in the STM image shown in (a). The STS spectra for these points are shown in (b) and the measured band gap as a function of distance from the step edge is plotted in (c). These experimental data

are compared to the calculated DOS of a stoichiometric zigzag edge at various distances from the edge as shown in (d). The band dispersion of this edge is shown in (e) with spin-up and spin-down edge states (red and blue) splitting close to Fermi-level at the X-point of the 1D Brillouin zone.

The stoichiometric zigzag edge is the only edge reliably observed in the PtSe$_2$ monolayer samples and thus it is the most relevant edge for the applications of PtSe$_2$. The edges are the terminations of 2D-crystals and thus are always present in finite size 2D islands. In contrast, under thermodynamic equilibrium, point defects will have a measurable concentration only at elevated temperatures. MBE grown samples are, however, usually not in thermodynamic equilibrium. Non-equilibrium defect structures are also frequently observed in other synthetic materials[45] including PtSe$_2$,[46,47] as defects formed under non-stoichiometric conditions or at high temperatures may not have enough time to reach the equilibrium concentration. Nevertheless, formation energies of different defects should still correlate with their abundance and may give an initial hint at the types of possible defects present in the MBE-grown samples. The observed point-defects in PtSe$_2$ monolayers and their relations to calculated formation energies are discussed next.

2.2 Point defects

Several point defects are observed in the MBE-grown PtSe$_2$ monolayers. Contrast modulation in the STM images generally extends over several unit cells indicating delocalization of the defect-induced states over a finite length. Imaging contrast is particularly pronounced when imaging with bias voltages within or close to the band gap of the monolayer PtSe$_2$. Under these conditions, the semiconducting basal planes are essentially transparent to the tunneling electrons and only tunneling from defect-induced electronic states contributes to the image contrast. Also, at low bias voltages the basal plane exhibits an apparent 2×2 periodicity for the PtSe$_2$/HOPG van der Waals heterostructure, as discussed previously.[35] The corresponding coincidence of the lattice constants of 2 x a$_{PtSe2}$= 3 x a$_{HOPG}$ suggest that the apparent periodicity is due to a resonant tunneling effect by the match between the Pt-dichalcogenide with the HOPG substrate, but may not correspond to a true topographic corrugation. DFT calculations indicate that the interaction between HOPG and Pt-dichalcogenides is minimal and does not induce any structural distortion of the planar Pt-dichalcogenides.[35]

To help identifying point defects in PtSe$_2$, we first consider their formation energies obtained in the DFT calculations. The formation energies for different possible point defects as functions of selenium chemical potential are presented in Figure 5. Se-vacancies (V$_{Se}$) have a low formation energy over a wide range of

Se chemical potential and thus their presence should be expected. Similarly, antisite defects with either Se at Pt-sites (Se_{Pt}) or Pt at Se-sites (Pt_{Se}) have low formation energies with a stronger dependence on the chemical potential. A defect with Pt and Se exchanging sites (Se_{Pt}-Pt_{Se}) is also considered, but such a defect involving the exchange of two atoms is high in energy and thus unlikely to form. Lastly, Pt-vacancies (V_{Pt}) have also a high formation energy, but during MBE growth under non-stoichiometric conditions such defects may form and thus it is plausible to observe V_{Pt}.
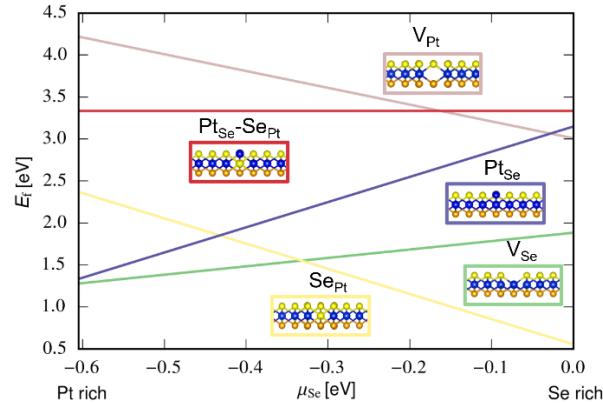

Figure 5: Formation energies as functions of Se chemical potential for various point defects in PtSe$_2$. These point defects include Se-vacancy (V_{Se}), Pt-vacancy (V_{Pt}), Se antisite (Se_{Pt}), Pt antisite (Pt_{Se}), and Se and Pt exchanging sites (Pt_{Se}-Se_{Pt}).

To identify the location of point defects in the samples, the center of the defect is determined first with respect to the atomic corrugation in the STM images (see supporting information Figure S2). Simulated STM images for the pristine surface indicates that the Se atoms in the topmost surface layer appear as protrusions over a wide range of bias voltages and thus the top-Se atoms are making up the sublattice imaged in the STM experiments. Using this Se sublattice, we pin-point if the center falls on the Se-site or in between three top Se-sites, which then could correspond to a Pt-site or a bottom Se site (*i.e.*, a Se-atom in the lower layer towards the graphite substrate) in the 1T structure. We also account for the abundance of defects according to their formation energy.

Figure 6 show STM images at different bias voltages of the most abundant defect in PtSe$_2$. The center of this defect is on the surface Se-site, which is particularly apparent at high negative voltages when the defect is imaged as a single depression. Experimental STS spectra in Fig. 6 (i) are compared with the computed density of states (DOS) plots shown in Fig. 6 (j). Both spectra of the pristine basal plane as well as spectra at the defects are displayed. The dI/dV spectrum of the basal plane shows the 1.8 eV band gap

of the pristine monolayer with the band edges indicated by the blue dashed lines in Fig 6 (i). Since DFT calculations with semilocal exchange and correlation functionals normally underestimate the band gap as compared to the experimentally measured gap, the DOS spectrum shown in Fig 6 (j) is stretched in order for the band edges of the pristine sample (indicated by $E_g(PtSe_2)$ in Fig. 6 (j)) to align with the experimental edges. While the energy scales for the experiment are different from those of the DFT calculations due to the underestimation of the gap, the alignment of the band edges allows for a direct visual comparison of the defect induced states in the experiments with the calculated ones. The same alignment has been performed for all the other defect structures discussed below. Comparison of the STS spectrum of a pristine monolayer $PtSe_2$ with a spectrum taken over the defect indicate an upward shift of the VBM and the formation of distinct gap states close to the VBM. These states agree with those calculated for Se vacancies. However, there are additional states in the calculations closer to the CBM that are not clearly observed in the experiments. The suppression of these states in the experimental STS spectrum may be because these states lie close to the experimental Fermi-level where the dI/dV spectra approach zero. Previous work on sulfur vacancies in WS_2,[48] have revealed that taking spin-orbit coupling (SOC) into account may give rise to the splitting of defect-induced levels in DFT calculations. The results for calculations of the DOS with account for SOC are presented in Fig. S3. It is evident that although some levels were indeed split, the account for SOC did not qualitatively change the picture. We note that the difference should be even smaller if the artificial broadening of the levels is introduce to match the experimental situation. Simulated STM images are in reasonably good agreement with the experimental observation. The center triangular or ring structure and the six bright protrusions arranged in a hexagon surrounding the defect are clearly reproduced in calculations of the occupied state images. A single depression is predicted for empty state images, which is observed experimentally at +1V bias. Thus, we assign this most abundant defect to Se-vacancies in the top layer. The electronic structure characterization shows that this defect mostly has defect states close to the VBM, but the contrast in the STM image indicates that these states can be delocalized over several atoms, with the hexagonal protrusions being three lattice constants away from the vacancy.
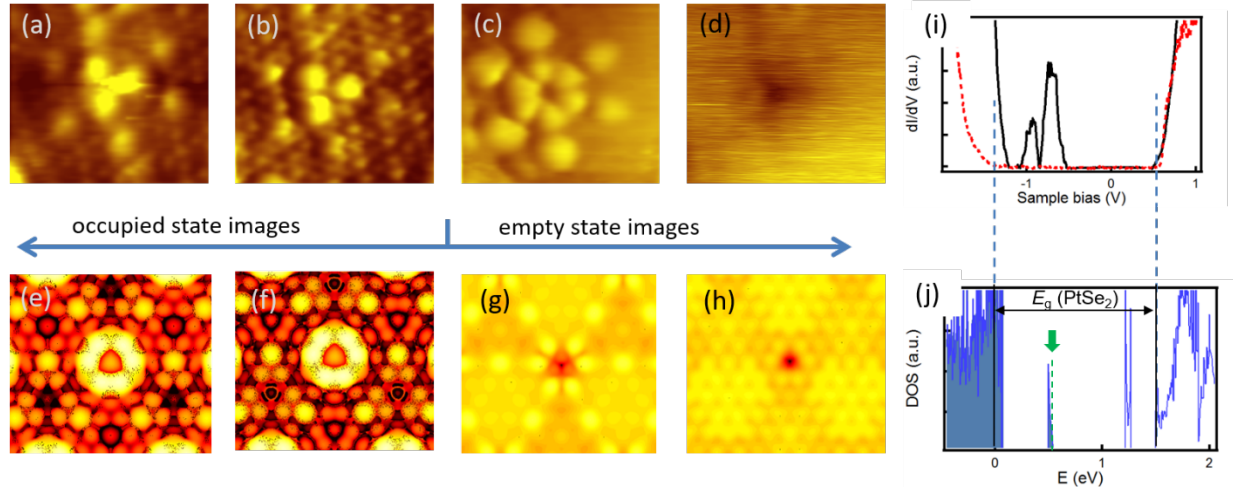
Figure 6: Characterization of Se-vacancies in the top-layer of PtSe$_2$. STM images for different bias voltages are shown in (a)-(d) and these can be compared to simulated STM images for occupied and empty states shown in (e)-(h). STS measurements at the defect (black solid line) are shown in (i) together with a spectrum taken on a pristine defect free PtSe$_2$ site (red dashed line). The calculated DOS at the defect site is shown in (j). The STS spectra and DOS calculations have been scaled for the band edges of the pristine sample (indicated by the blue dashed line in (i) and (j)) to coincide in order to facilitate comparison of the calculations with the experiment. The VBM of the pristine PtSe$_2$ surface is set to zero eV and the highest occupied e defect state is indicated by the green arrow.

Figure 7 shows a less frequent defect, whose center is in between the chalcogen surface atoms. The STS of this defect is similar to the STS of the chalcogen vacancies (Figure 6 (i)), with two pronounced band gap states close to the VBM and an upward shift of the VBM as compared to the pristine PtSe$_2$. This suggests that this defect may also be a Se vacancy but located at the side of the PtSe$_2$ sheet facing the substrate, *i.e.*, away from the surface in the bottom layer of PtSe$_2$. Obviously, the calculated DOS for a Se-vacancy in the bottom-layer is the same as for the top-layer and thus is not reproduced in Figure 7. The STM images also exhibit a similar size of the defect structure as for the top-Se vacancies, but with a clearly different appearance. Under empty state imaging conditions (+1V) the defect exhibits a triangular depression that extends over three surface Se-sites. Imaging filled states (but still within the band gap of monolayer PtSe$_2$) at -1V bias, the defects exhibit a complex contrast. Both the empty and filled state STM images are again well reproduced in the simulated images for a bottom layer Se-vacancy. Note that using a larger supercell in the calculations reveals additional structure that is in better agreement with the experiment. Consequently, STM images of this defect are assigned to the bottom layer Se-vacancies. It is interesting to note that these defects are less frequent than the top layer Se-vacancies. This indicates that the

graphite substrate plays an important role in the Se-vacancy formation, with Se-vacancies on the surface of PtSe$_2$ favored over Se-vacancies at the interface with the substrate.
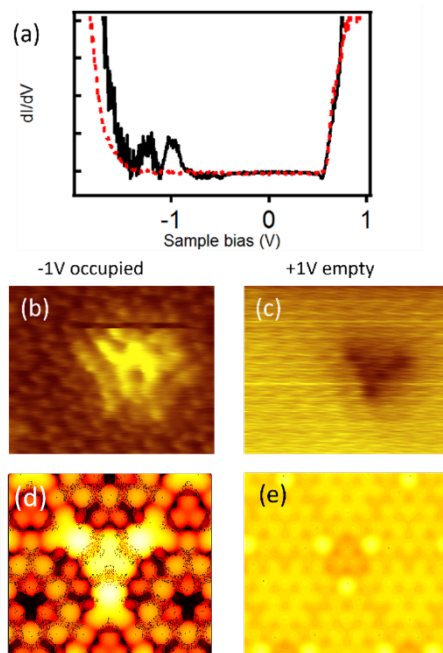

Figure 7: Characterization of Se-vacancy in the bottom layer of PtSe$_2$. STS spectrum measured on this defect is shown in (a) as the black line together with the spectrum on a defect free PtSe$_2$ region (shown as red-dashed line). STM images at 1V negative and positive bias is shown in (b) and (c), respectively and this can be compared to simulated STM images of occupied and empty states shown in (d) and (e), respectively.

Figure 8 shows STM and DFT analysis of a defect that is assigned to Pt-vacancies. This assignment is based on the location of the center of the defect in between the top-most Se-atom sites, but mostly based on the comparison between experimental STM/STS and DFT results. DOS calculations for Pt-vacancies indicate that such point defects have strong band gap states. Moreover, these band gap states are spin-polarized, as shown in Figure 8 (j), and this may be important for the observed magnetic properties in this material.[12,13] Additional calculations including SOC can be found in Fig. S3. Strong defect states are also found in the experimental STS. The defect exhibits states at the VBM, and several band gap-states that can be correlated to the calculated states. In addition to the STS, STM images are also in good agreement with the calculated STM images. The experimental STM images for both positive and negative bias voltages can be described as three bright protrusions in the center with six less bright 'rays' radially going outwards from the center. These features are well-reproduced in the simulated images.
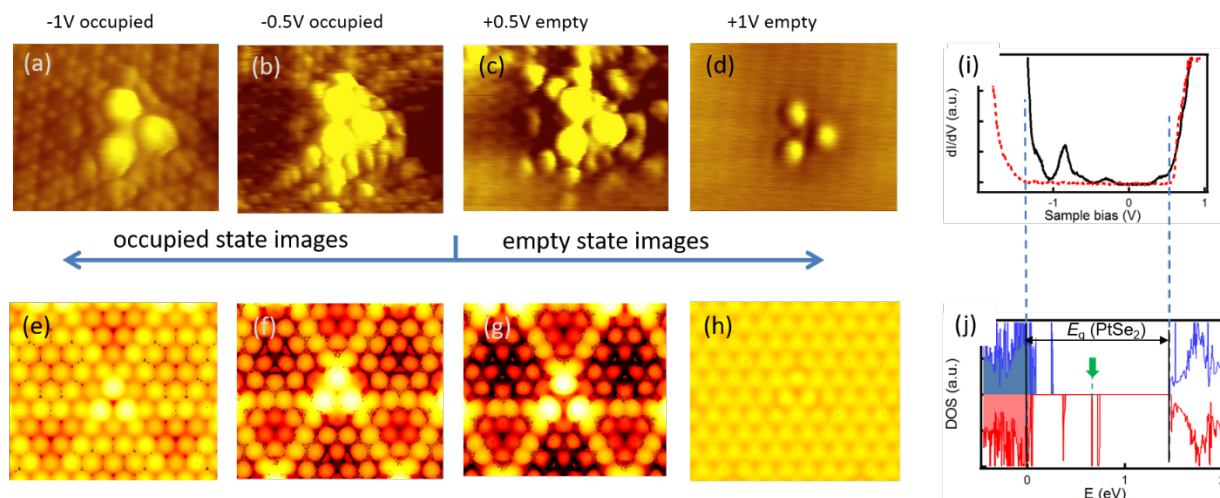
Figure 8: Characterization of Pt-vacancy in PtSe$_2$. STM images for different bias voltages are shown in (a)-(d) and these can be compared to the simulated STM images for occupied and empty states shown in (e)-(h). STS measurements at the defect (black solid line) are presented in (i) together with a spectrum taken on a pristine defect-free PtSe$_2$ site (red dashed line). The calculated DOS at the defect site is shown in (j) with spin-up and spin-down states indicated by red and blue. The STS spectra and DOS calculations have been scaled for the band edges of the pristine sample (indicated by the blue dashed line in (i) and (j)) to coincide in order to facilitate comparison of the calculations with the experiment. The VBM of the pristine PtSe$_2$ surface is set to zero eV and the highest occupied e defect state is indicated by the green arrow.

Finally, we observe another defect that appears to be centered in between the surface Se-atoms. This defect only exhibits clear contrast for bias voltages corresponding to the band gap region of the PtSe$_2$ basal plane, as shown in Figure 9. In STS, this defect has no strong band gap states, Figure 9 (g) but may have some additional states at the CBM. We assign this defect to a Se$_{Pt}$ antisite, *i.e.*, a Se atom occupying a Pt lattice site. One main reason for this assignment is the lack of band gap states in the experiments, which is reproduced by the DFT calculations. This lack of defect-induced states also explains the weak imaging contrast in STM, which is also reproduced in calculated images. Only for imaging conditions close to the VBM a three-lobe structure is observed which is similar to the structure seen in calculated images of Se$_{Pt}$ antisite defects.
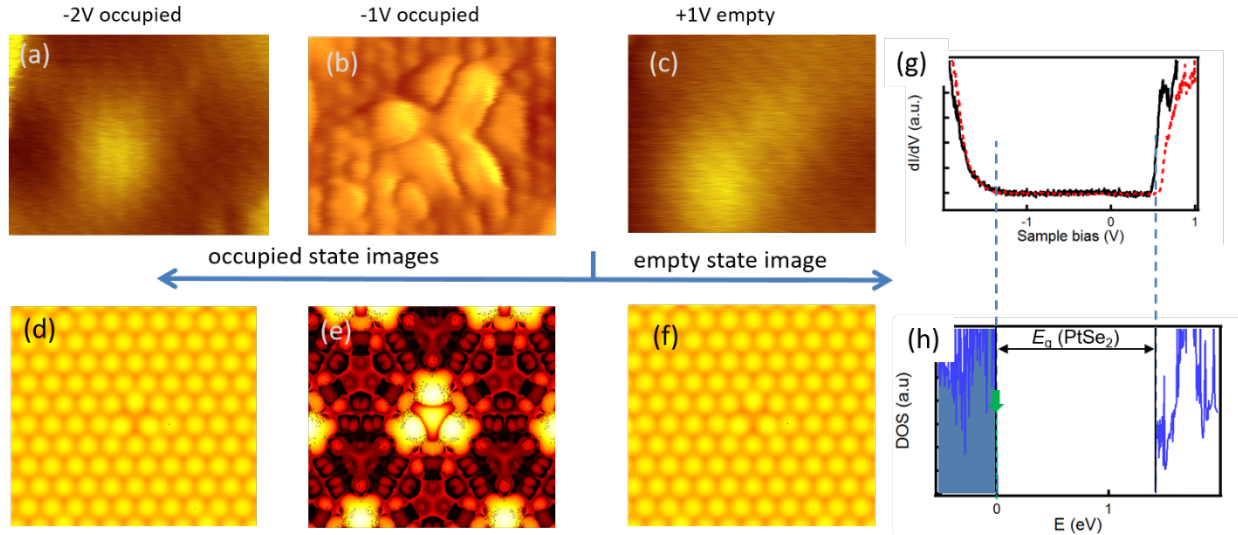
-2V occupied   -1V occupied   +1V empty

(a)   (b)   (c)   (g)

occupied state images   empty state image

(d)   (e)   (f)   (h)

Figure 9: Characterization of Se$_{Pt}$ antisite (Se occupying Pt lattice sites). STM images for different bias voltages are shown in (a)-(c). Only for bias voltage in the band gap (-1V) a clear contrast can be seen for this defect. This is consistent with the simulated STM images shown in (d)-(f). The STS spectra shown in (g) indicates the absence of pronounced band gap states for this defect, also consistent with the calculated DOS shown on (h). The VBM of the pristine PtSe$_2$ surface is set to zero eV and the highest occupied e defect state is indicated by the green arrow.

Thus, MBE-grown PtSe$_2$ monolayers exhibit three common point defects. Se-vacancies are most frequent, which agrees with their relatively low formation energy. It is interesting though that their formation seems to be suppressed at the interface with graphite. At the Pt-site we observe two defects. If the Pt-site is occupied by Se (Se-antisite), almost no additional band gap states are observed and thus does not alter the band gap of monolayer PtSe$_2$. In contrast, if the Pt-site is empty (Pt-vacancy) high density of band gap states are observed. Other intrinsic point defects, as well as substitutional impurity atoms such as oxygen, carbon, and hydrogen that were not observed in the experiments but were calculated can be found in Figures S4- S10.

A statistical analysis of the different point defects in our samples give an estimate of their concentration. As pointed out the Se-vacancies are by far the most frequently observed defects with a concentration of ~ 4×10^{-12} cm^{-2} or one defect per 5×5 nm^2 area. The Pt-vacancies and Se$_{Pt}$ antisites are almost an order of magnitude less likely to be observed in our samples with concentrations of ~ 3×10^{-11} cm^{-2} or roughly one defect per 20×20 nm^2 area. The much higher concentration of the Se-vacancies is consistent with our *ab-initio* thermodynamic calculations; however, we should be cautious of comparing the equilibrium

16

thermodynamic concentration of defects obtained from zero-temperature DFT calculations with the actual concentration of defects in the samples grown using MBE. Thin films growth is often controlled by kinetic effects, and the samples do not have enough time to reach equilibrium. It is interesting to note, though, that the very low Pt vacancy concentrations we found in our samples are in good agreement with those reported from transmission electron microscopy analysis of CVD grown $PtSe_2$ multilayers.[49] This may indicate that similar Pt-vacancy concentrations are obtained by different growth methods and that these are generally very sparse.

3. Conclusions

DFT calculations indicate that zigzag edges with a stoichiometric termination are energetically preferable in good agreement with the experimental results. While surface states in extended materials are 2D, edge states of planar materials are confined in 1D. This may give these metallic edge-states electronic properties described by the Tomonaga Luttinger liquid theory,[50] which has been shown for other edge states[19] and line defects in 2D materials.[51,52] Interestingly, electronic structure calculations predict that the stoichiometric zigzag edges of $PtSe_2$ have spin polarized bands with different band gaps (small gap of about 0.1 eV in one channel), which suggests 1D magnetic states and spin gapless semiconductor[53] behavior, which may have applications in spintronics. This warrants further fundamental studies of the electronic properties of metallic edge states in Pt-dichalcogenides. Edges in 2D materials also have often been assigned to special catalytic properties and the changed electronic structure of $PtSe_2$ edges also implies varied chemical properties. However, to assess the chemical functionalities further, the stability of the edge configurations under ambient conditions needs to be considered, which cannot be reliably evaluated in the UHV studies presented here. For the point defects, chalcogen vacancies have been identified to be the most frequently observed defect in the MBE-grown samples, consistent with the results of *ab initio* calculations that show the Se vacancies have a low formation energy over a large range of Se chemical potential. In addition to other low energy defects, namely Se-antisites, *i.e.*, Se occupying Pt-sites, Pt vacancies are also observed, despite their relatively high formation energy. The high energy indicates that these are not thermodynamic equilibrium defects but rather must be a consequence of the sample preparation that kinetically traps some Pt-vacancies. In general imaging of defects by STM with bias voltages within or close to the band gap of the monolayer is enabled by the conducting graphite substrate. This imaging allows to visualize the extent of the defect states over many lattice constants. Defect states in the monolayer band gap or close to the band edges are observed for all point defects giving rise to pronounced contrast in STM images at low bias voltages. Pt-vacancies exhibit the most

17

pronounced defect states that give rise to a significant closing of the band gap. Interestingly, spin polarized DFT simulations also indicate that this defect is the only one with strong spin-polarized defect states and thus is consistent with previous reports[12,13] that associated the observed magnetic properties in PtSe$_2$ with such defects. However, it is still debated if these very dilute Pt-vacancies can couple magnetically and give rise to long range magnetic ordering.[49] Moreover, the low density of these defects and their high formation energy suggest that this is a kinetically trapped defect, formed during non-equilibrium growth processes. Thus, tuning magnetism in PtSe$_2$ by the controllable formation of Pt vacancies during the growth may be difficult to achieve. Post-synthesis methods, e.g., ion or electron irradiation, can hardly be used either, as they give mostly rise to chalcogen vacancies in TMDs.[54,55] Therefore, the magnetic properties may be more reliably tailored by doping with impurities[56,57] rather than by introducing intrinsic defects. On the other hand, the spin polarized edge states are exciting for tuning magnetic properties in PtSe$_2$ monolayer ribbons and other nanostructures, and these edge properties should be studied further also in transport measurements.

4. Experimental and Computational Section

Experimental: PtSe$_2$ islands are grown on freshly cleaved HOPG substrates by MBE growth. Prior to the growth the substrates are outgassed in vacuum at 450 ˚C for ~12 hours. Pt and Se are co-deposited in ultra-high vacuum (UHV). The Pt was evaporated from a solid 2mm Pt-wire in a mini- e-beam evaporator and the Se was evaporated from a Knudsen cell. The deposition-rate ratio of Se:Pt was more than 10:1 and the growth rate was very slow at ~1/3 ML per hour. During growth the substrate was held at a temperature of ~ 250 ˚C. After growth the sample was transferred to a cryogenic STM cooled with a closed cycle cryostat. The STM and STS studies were performed at a temperature of 100 K with electrochemically etched tungsten wires. For STS the tips were characterized on bare terraces of the HOPG substrate. The STS measurement were recorded with a lock-in amplifier with a 30 mV modulation voltage.

Computational: The energetics and electronic structure of all point defects and edges were studied using spin-polarized density functional theory (DFT) as implemented in the VASP code.[58,59] All the calculations were conducted using PBE exchange-correlation functional.[60] The structures are fully optimized with an energy cut-off of 600 eV and a force tolerance of 0.01 eVA^{-1}. The point defects are modeled using a 6x6 supercell composed of 108 atoms with a vacuum space of 20 Å in the confinement direction. A larger rectangular supercell composed of 523 atoms were also used for the simulations of the STM images of vacancies. The Brillouin zone of the systems was sampled using 3x3x1 Monkhorst-Pack grid for point defects and 8x1x1 grid for edge models. For electronic structure calculations, the Brillouin zone was

sampled using 9x9x1 k-points and 8x1x1 k-points for point defects and edge structures, respectively. Constant current STM images are simulated using the Tersoff-Hamann approximation.

Supporting Information:

Supporting information is available from Wiley Online Library of from the author.

Conflict of interest:

The authors declare no conflict of interest.

References:

[1] G. Wang, Z. Wang, N. McEvoy, P. Fan, W.J. Blau, *Adv. Mater.* **2021**, *33*, 2004070.

[2] E. Chen, W. Xu, J. Chen, J.H. Warner, *Mater. Today Adv.* **2020**, *7*, 100076.

[3] X. Chia, A. Adriano, P. Lazar, Z. Sofer, J. Luxa, M. Pumera, *Adv. Funct. Mater.* **2016**, *26*, 4306-4318.

[4] N.F. Rosli, C.C. Mayorga-Martinez, N.M. Latiff, N. Rohaizad, Z. Sofer, A.C. Fisher, M. Pumera, *ACS Sustain. Chem. Eng.* **2018**, *6*, 7432–7441.

[5] H. Huang, X. Fan, D.J. Singh, W. Zheng, *ACS Omega* **2018**, *3*, 10058–10065.

[6] S. Wagner, C. Yim, N. McEvoy, S. Kataria, V. Yokaribas, A. Kuc, S. Pindl, C.-P. Fritzen, T. Heine, G.S. Duesberg, M.C. Lemme, *Nano Lett.* **2018**, *18*, 3738.

[7] M. Sajjad, E. Montes, N. Singh, U. Schwingenschlögl, *Adv. Mater. Interfaces* **2017**, *4*, 1600911.

[8] C. Yim, K. Lee, N. McEvoy, M. O'Brien, S. Riazimehr, N.C. Berner, C.P. Cullen, J. Kotakoski, J.C. Meyer, M.C. Lemme, G.S. Duesberg, *ACS Nano* **2016**, *10*, 9550–9558.

[9] Z. Wang, Q. Li, F. Besenbacher, M. Dong, *Adv. Mater.* **2016**, *28*, 10224–10229.

[10] Y. Zhao, J. Qiao, Z. Yu, P. Yu, K. Xu, S.P. Lau, W. Zhou, Z. Liu, X. Wang, W. Ji, Y. Chai, *Adv. Mater.* **2017**, *29*, 1604230.

[11] T. Das, E. Yang, J.E. Seo, J.H. Kim, E. Park, M. Kim, D. Seo, J.Y. Kwak, J. Chang, *ACS Appl. Mater. Interfaces* **2021**, *13*, 1861–1871.

[12] A. Avsar, A. Ciarrocchi, M. Pizzochero, D. Unuchek, O.V. Yazyev, A. Kis, *Nat. Nanotechnol.* **2019**, *14*, 674–678.

[13] A. Avsar, C.-Y. Cheon, M. Pizzochero, M. Tripathi, A. Ciarrocchi, O.V. Yazyev, A. Kis, *Nat. Commun.* **2020**, *11*, 4806.

[14] X. Li, Y. Fang, J. Wang, H. Fang, S. Xi, X. Zhao, D. Xu, H. Xu, W. Yu, X. Hai, C. Chen, C. Yao, H.B. Tao, A.G.R. Howe, S.J. Pennycook, B. Liu, J. Lu, C. Su, *Nat. Commun.* **2021**, *12*, 2351.

[15] S. Lina, Y. Liua, Z. Hub, W. Luc, C.H. Maka, L. Zenga, J. Zhaoa, Y. Lia, F. Yana, Y.H. Tsanga, X. Zhanga, S.P. Lau. *Nano Energy* **2017**, *42*, 26–33.

[16] J. Hong, Z. Hu, M. Probert, K. Li, D. Lv, X. Yang, L. Gu, N. Mao, Q. Feng, L. Xie, J. Zhang, D. Wu, Z. Zhang, C. Jin, W. Ji, X. Zhang, J. Yuan, Z. Zhang, *Nat. Commun.* **2015**, *6*, 6293.

[17] M.V. Bollinger, J.V. Lauritsen, K.W. Jacobsen, J.K. Nørskov, S. Helveg, F. Besenbacher, *Phys. Rev. Lett.* **2001**, *87*, 196803.

[18] C. Zhang, A. Johnson, C.-L. Hsu, L.-J. Li, C.-K. Shih, *Nano Lett.* **2014**, *14*, 2443−2447.

[19] G. Yang, Y. Shao, J. Niu, X. Ma, C. Lu, W. Wei, X. Chuai, J. Wang, J. Cao, H. Huang, G. Xu, X. Shi, Z. Ji, N. Lu, D. Geng, J. Qi, Y. Cao, Z. Liu, L. Liu, Y. Huang, L. Liao, W. Dang, Z. Zhang, Y. Liu, X. Duan, J. Chen, Z. Fan, X. Jiang, Y. Wang, L. Li, H.-J. Gao, X. Duan, M. Liu, *Nat. Commun.* **2020**, *11*, 659.

[20] S. Tang, C. Zhang, D. Wong, Z. Pedramrazi, H.-Z. Tsai, C. Jia, B. Moritz, M. Claassen, H. Ryu, S. Kahn, J. Jiang, H. Yan, M. Hashimoto, D. Lu, R.G. Moore, C.-C. Hwang, C. Hwang, Z. Hussain, Y. Chen, M.M. Ugeda, Z. Liu, X. Xie, T.P. Devereaux, M.F. Crommie, S.-K. Mo, Z.-X. Shen. *Nat. Phys.* **2017**, *13*, 683.

[21] P. Chen, W.W. Pai, Y.-H. Chan, W.L. Sun, C.-Z. Xu, D.-S. Lin, M.Y. Chou, A.V. Fedorov, T.-C. Chiang, *Nat. Commun.* **2018**, *9*, 2003.

[22] X. Qian, J. Liu, L. Fu, J. Li, *Science* **2014**, *346*, 1344

[23] K. Lasek, J. Li, S. Kolekar, P.M. Coelho, M. Zhang, Z. Wang, M. Batzill, *Surf. Sci. Rep.* **2021**, *76*, 100523.

[24] J.A. Wilson, A.D. Yoffe, *Adv. Phys.* **1969**, *18*,193-335.

[25] S. Manzeli, D. Ovchinnikov, D. Pasquier, O.V. Yazyev, A. Kis, *Nat. Rev. Mater.* **2017**, *2*, 17033.

[26] K.F. Mak, C. Lee, J. Hone, J. Shan, T.F. Heinz, *Phys. Rev. Lett.* **2010**, *105*, 136805.

[27] S. Kolekar, M. Bonilla, Y. Ma, H.C. Diaz, M. Batzill, *2D Mater.* **2017**, *5*, 015006.

[28] P. Chen, W.W. Pai, Y.-H. Chan, A. Takayama, C.-Z. Xu, A. Karn, S. Hasegawa, M.Y. Chou, S.-K. Mo, A.-V. Fedorov, T.-C. Chiang, *Nat. Commun.* **2017**, *8*, 516.

[29] P.M. Coelho, K.N. Cong, M. Bonilla, S. Kolekar, M.-H. Phan, J. Avila, M.C. Asensio, I.I. Oleynik, M. Batzill, *J. Phys. Chem. C* **2019**, *123*, 14089-14096.

[30] G. Duvjir, B.K. Choi, I. Jang, S. Ulstrup, S. Kang, T.T. Ly, S. Kim, Y.H. Choi, C. Jozwiak, A. Bostwick, E. Rotenberg, J.-G. Park, R. Sankar, K.-S. Kim, J. Kim, Y.J. Chang, *Nano Lett.* **2018**, *18*, 5432–5438.

[31] P.M. Coelho, K. Lasek, K.N. Cong, J. Li, W. Niu, W. Liu, I.I. Oleynik, M. Batzill. *J. Phys. Chem. Lett.* **2019**, *10*, 4987-4993.

[32] M.M. Ugeda, A.J. Bradley, Y. Zhang, S. Onishi, Y. Chen, W. Ruan, C. Ojeda Aristizabal, H. Ryu, M.T. Edmonds, H.-Z. Tsai, A. Riss, S.-K. Mo, D. Lee, A. Zettl, Z. Hussain, Z.-X. Shen, M.F. Crommie. *Nat. Phys.* **2016**, 12, 92-97.

[33] X. Xi, L. Zhao, Z. Wang, H. Berger, L. Forró, J. Shan, K.F. Mak. *Nat. Nanotechnol.* **2015**, *10*, 765–769.

[34] Y. Chen, W. Ruan, M. Wu, S. Tang, H. Ryu, H.-Z. Tsai, R. Lee, S. Kahn, F. Liou, C. Jia, O.R. Albertini, H. Xiong, T. Jia, Z. Liu, J.A. Sobota, A.Y. Liu, J.E. Moore, Z.-X. Shen, S.G. Louie, S.-K. Mo, M.F. Crommie. *Nat. Phys.* **2020**, *16*, 218–224.

[35] J. Li, S. Kolekar, M. Ghorbani-Asl, T. Lehnert, J. Biskupek, U. Kaiser, A.V. Krasheninnikov, M. Batzill. *ACS Nano* **2021**, *15*, 13249–13259.

[36] A. Ciarrocchi, A. Avsar, D. Ovchinnikov, A. Kis, *Nat. Commun.* **2018**, *9*, 919.

[37] R.A.B. Villaos, C.P. Crisostomo, Z.-Q. Huang, S.M. Huang, A.A.B. Padama, M.A. Albao, H. Lin, F.-C. Chuang, *npj 2D Mater. Appl.* **2019**, *3*, 2.

[38] Y. Zhao, J. Qiao, P. Yu, Z. Hu, Z. Lin, S.P. Lau, Z. Liu, W. Ji, Y. Chai, *Adv. Mater.* **2016**, *28*, 2399–2407.

[39] Y. Zhao, J. Qiao, Z. Yu, P. Yu, K. Xu, S.P. Lau, W. Zhou, Z. Liu, X. Wang, W. Ji, Y. Chai, *Adv. Mater.* **2017**, *29*, 1604230.

[40] L. Ansari, S. Monaghan, N. McEvoy, C.Ó. Coileáin, C.P. Cullen, J. Lin, R. Siris, T. Stimpel-Lindner, K.F. Burke, G. Mirabelli, R. Duffy, E. Caruso, R.E. Nagle, G.S. Duesberg, P.K. Hurley, F. Gity, *npj 2D Mater. Appl.* **2019**, *3*, 33.

[41] S. Liu, Z. Liu, *Phys. Chem. Chem. Phys.* **2018**, *20*, 21441-21446.

[42] J.P. Perdew, K. Burke, M. Ernzerhof, *Phys. Rev. Lett.* **1996**, *77*, 3865.

[43] Y.L. Huang, Y. Chen, W. Zhang, S.Y. Quek, C.-H. Chen, L.-J. Li, W.-T. Hsu, W.-H. Chang, Y.J. Zheng, W. Chen, A.T.S. Wee, *Nat. Commun.* **2015**, *6*, 6298.

[44] Y. Ma, S. Kolekar, H.C. Diaz, J. Aprojanz, I. Miccoli, C. Tegenkamp, M. Batzill, *ACS Nano* **2017**, *11* 5130–5139.

[45] Z. Lin, B.R. Carvalho, E. Kahn, R. Lv, R. Rao, H. Terrones, M.A. Pimenta, M. Terrones, *2D Mater.* **2016**, *3*, 022002.

[46] H. Zheng, Y. Choi, F. Baniasadi, D. Hu, L. Jiao, K. Park, C. Tao, *2D Mater.* **2019**, *6*, 041005.

[47] J. Chen, Y. Wang, W. Xu, Y. Wen, G.H. Ryu, J.C. Grossman, J.H. Warner, *ACS Nano* DOI: 10.1021/acsnano.1c06736.

[48] B. Schuler, D.Y. Qiu, S. Refaely-Abramson, C. Kastl, C.T. Chen, S. Barja, R.J. Koch, D.F. Ogletree, S. Aloni, A.M. Schwartzberg, J.B. Neaton, S.G. Louie, A. Weber-Bargioni, *Phys. Rev. Lett.* **2019**, *123*, 076801.

[49] J. Ge, T. Luo, Z. Lin, J. Shi, Y. Liu, P. Wang, Y. Zhang, W. Duan, J. Wang, *Adv. Mater.* **2021**, *33*, 2005465.

[50] J. Voit, *Rep. Prog. Phys.* **1995**, *58*, 977-1116.

[51] Y. Ma, H.C. Diaz, J. Avila, C. Chen, V. Kalappattil, R. Das, M.-H. Phan, T. Čadež, J.M.P. Carmelo, M.C. Asensio, M. Batzill, *Nat. Commun.* **2017**, *8*, 14231.

[52] W. Jolie, C. Murray, P.S. Weiß, J. Hall, F. Portner, N. Atodiresei, A.V. Krasheninnikov, C. Busse, H.-P. Komsa, A. Rosch, T. Michely, *Phys. Rev. X* **2019**, *9*, 011055.

[53] X.L. Wang *Phys. Rev. Lett.* **2008**, *100*, 156404.

[54] M. Ghorbani-Asl, S. Kretschmer, D.E. Spearot, A.V. Krasheninnikov, *2D Mater.* **2017**, *4*, 025078

[55] H.-P. Komsa, J. Kotakoski, S. Kurasch, O. Lehtinen, U. Kaiser, A.V. Krasheninnikov, *Phys. Rev. Lett.* **2012**, *109*, 35503.

[56] W. Chen, J.-m. Zhang, X.-g. Wang, Q.-l. Xia, Y.-z. Nie, G.-h. Guo, *J. Mag. Mag. Mater.* **2021**, *518*, 167433.

[57] M. Kar, R. Sarkar, S. Pal, P. Sarkar, *J. Phys.: Condens. Matter* **2019**, *31*, 145502.

[58] G. Kresse, J. Furthmüller, *Phys. Rev. B* **1996**, *54*, 11169.

[59] G. Kresse, J. Furthmüller, *Comp. Mater. Sci.* **1996**, *6*, 15-50.

[60] J.P. Perdew, K. Burke, M. Ernzerhof, *Phys. Rev. Lett.* **1996**, *77*, 3865.